Biosensors and Bioelectronics 203 (2022) 114038

Contents lists available at ScienceDirect

Biosensors and Bioelectronics

journal homepage: www.elsevier.com/locate/bios

Exploring near-field sensing efficiency of complementary plasmonic metasurfaces for immunodetection of tumor markers

Fajun Li [a,b,1], Jiaqing Shen [a,1], Chaoheng Guan [a], Yinong Xie [a], Zhenbiao Wang [a], Shaowei Lin [c], Junjie Chen [d], Jinfeng Zhu [a,b,*]

[a] Institute of Electromagnetics and Acoustics and Key Laboratory of Electromagnetic Wave Science and Detection Technology, Xiamen University, Xiamen, 361005, China
[b] State Key Laboratory of Applied Optics, Changchun Institute of Optics, Fine Mechanics and Physics, Chinese Academy of Sciences, Changchun, 130033, China
[c] The First Affiliated Hospital of Xiamen University, Xiamen, 361003, China
[d] Analysis and Measurement Center, School of Pharmaceutical Science, Xiamen University, Xiamen, 361003, China

ARTICLE INFO

Keywords:
Complementary metasurfaces
Surface sensitivity
Plasmonic biosensors
Near-field enhancement
Cancer biomarkers
Point-of-care testing

ABSTRACT

Plasmonic metasurface biosensors have great potential on label-free high-throughput clinical detection of human tumor markers. In the past decades, nanopillar and nanohole metasurfaces have become the common choices for plasmonic biosensing, because they typically enable universal simple large-area nanopatterns via a low-cost reproducible fabrication manner. The two kinds of metasurfaces have the complementary shapes and are used to be assumed as the same type of two-dimensional plasmonic nanograting for biosensing. Up to date, there is still a lack of comparison study on their biosensing performance, which is critical to guide their better applications on tumor marker detection. In this study, we compare the bulk/surface refractive index and sensitivity of plasmonic nanopillar (PNP) and plasmonic nanohole (PNH) metasurfaces in order to evaluate their biosensing capabilities. The sensing physics about their space near-field utilization is systematically revealed. The PNH metasurface demonstrates a higher biomolecule sensitivity versus the complementary PNP metasurface, and its limit of detection for bovine serum albumin reaches ~0.078 ng/mL, which implies a greater potential of detecting cancer biomarkers. We further adopt the PNH metasurfaces for immunoassay of three typical tumor markers by testing clinical human serum samples. The results imply that the immunodetection of alpha-fetoprotein has the most optimal sensing efficiency with the lowest detection concentration (<5 IU/mL), which is much lower than its clinical diagnosis threshold of ~16.5 IU/mL for medical examination. Our work has not only illuminated the distinct biosensing properties of complementary metasurfaces, but also provided a promising way to boost plasmonic biosensing for point-of-care testing.

1. Introduction

Plasmonic metasurface biosensor is a kind of optical refractive index sensing device, on which the environmental biomolecular binding can be detected by the change of spectral response (He et al., 2021; Spitzberg et al., 2019). Its sensitivity highly depends on the plasmonic effects of local electric field enhancement surrounding the metasurface. Compared with the conventional prism-based plasmonic biosensor, it is a low-cost compact device for multiplex sensing of biomarkers by using a state-of-the-art fabrication process (Oh and Altug, 2018; Yesilkoy et al., 2018). It also implies promising potential on high-throughput label-free detection of tumor markers for the diagnosis and prognosis of cancer (Li et al., 2015; Wang et al., 2018). In the past few years, various plasmonic metasurface biosensors have been widely investigated (Belushkin et al., 2018; Liu et al., 2018; Siddique et al., 2019). Researchers usually improve the sensing performance by optimizing the shape of metaunit, such as nanocups (Huang et al., 2021), nanocheckerboard (Cai et al., 2019), nanoscale mushrooms (Shen et al., 2013), nanopyramids (Zhang et al., 2021), nanopillars (Ko et al., 2018; Lee et al., 2019; Chou Chao et al., 2020; Chau et al., 2019a), and nanoholes (Gao et al., 2020; Prasad et al., 2019). Among so many kinds of plasmonic metasurfaces, both nanopillars and nanoholes are the most common candidates for

* Corresponding author. Institute of Electromagnetics and Acoustics and Key Laboratory of Electromagnetic Wave Science and Detection Technology, Xiamen University, Xiamen, 361005, China.
E-mail address: nanoantenna@hotmail.com (J. Zhu).
[1] These authors contributed equally to this work.

https://doi.org/10.1016/j.bios.2022.114038
Received 7 October 2021; Received in revised form 20 January 2022; Accepted 21 January 2022
Available online 26 January 2022

developing plasmonic metasurface biosensors, because their simple periodic nanostructures facilitate the low-cost large-area fabrication by a reproducible process, which is especially significant for point-of-care-testing of tumor makers (Hackett et al., 2018; Zhu et al., 2020b). These two plasmonic metasurfaces have the complementary property in geometry, and their bulk refractive index sensitivity (BRIS) and surface refractive index sensitivity (SRIS) have been widely investigated to evaluate the potential biosensing applications (Im et al., 2014; Jiao et al., 2021; Ray et al., 2020; Vala et al., 2019). However, there is still a lack of systematic comparison studies on their optical biosensing performance, which is very important to determine their uses in tumor marker detection.

In the biomolecule detection by PNP and PNH metasurfaces, the use of SRIS is much more effective to evaluate the biosensing performance than BRIS. This is because the biomolecules (such as various tumor makers) usually have the nanoscale size, they are bound within a small limited range on the surface of nanostructures, and SRIS is a good sensor indicator to correlate the plasmonic near-field effects surrounding the metallic surface (Couture et al., 2012; Tobing et al., 2021). Conventionally, the physical definition of SRIS mainly takes into account the localized refractive index and the size of adsorbate versus the exponential decay length of optical field (Kedem et al., 2011; Li et al., 2015). In practice, the surface sensing procedures for biomolecule detection are usually more complicated. For instance, the detection of tumor markers is based on the mechanism of immunosensing, in which the nanopillar or nanohole plasmonic metasurface requires biofunctionalization with capture molecules. During the sensing process, these molecules can recognize and trap the target tumor makers by a specific binding interaction (Zhou et al., 2019). In fact, various tumor markers usually have large size differences, on which conditions the molecule size fitting with the enhanced near-field region of metasurface becomes quite in demand (Zhan et al., 2020; Zhu et al., 2020b). On the other hand, the capture molecules often occupy a certain near-field region, and their existence would influence the sensitivity to the target tumor makers (Špačková et al., 2016). These two aspects of immunosensors seriously affect the near-field sensing efficiency of PNP and PNH metasurfaces, so increasing the near-field utilization efficiency of plasmonic field modes for biomolecular detection is of great importance. Unfortunately, the related studies, especially on the detection efficiency for multiplex tumor markers, are barely performed and reported.

In this study, the complementary PNP and PNH metasurfaces are investigated and compared systematically. The PNH metasurfaces show higher BRIS and SRIS than PNP metasurfaces, which demonstrate the more promising biosensing performance. We adopt the capture molecules and target tumor markers with different sizes on the PNH metasurfaces, and find that the effective surface near-field utilization by selecting appropriate biomolecule types and sizes would lead to the most optimum biosensing performance. Our work illuminates a biomolecule-customized matching mechanism of plasmonic metasurfaces, which implies a promising potential for future clinical applications.

2. Experimental

2.1. Materials, fabrication and characterization

The positive poly(allylamine hydrochloride) (PAH, 65 kDa) solution (Sigma-Aldrich, Steinheim, Germany) and negative poly(sodium 4-styrene sulfonate) (PSS, 75 kDa) solution (Aladdin Biotechnology, Shanghai, China) are used for alternate assembly of polyelectrolyte bilayers. The alpha-fetoprotein (AFP), anti-AFP, carbohydrate antigen 50 (CA 50), anti-CA 50, carbohydrate antigen 19-9 (CA 19-9), and anti-CA 19-9, are from Siemens Healthcare Diagnostics (New York, USA). The PNP and PNH metasurfaces are fabricated simultaneously by nanoimprinting with the same nickel mold (see Section 1 in Supporting Material). We adopt the antibody/antigen specific binding of immunoassay for label-free detection of the tumor markers CA 19-9, CA 50 and AFP (see Section 2 in Supporting Material). The scanning electron microscope (SEM, Hitachi S-4800) is used to characterize the metasurface morphology. The energy dispersive spectroscopy combined with the SEM is adopted to obtain the mapping of nitrogen element content for metasurfaces (see Fig. S4 in Supporting Material).

2.2. Optical measurement and numerical simulation

A laboratory-built system, consisting of a light source, a UV-visible-NIR spectrometer, and an integrated optical fiber probe (Avantes BV, Netherlands), is used to measure the reflectance spectra of all samples. The BRIS is obtained by measuring the reflectance spectra in four solvents with the different values of refractive index n, respectively. The SRIS is obtained by measuring the reflectance spectra using the PAH and PSS bilayers in a layer-by-layer (LbL) assembly way (Mariani et al., 2018). For each measurement, the reflectance spectrum and the sensing performance of a sample are recorded three times (see Section 3 in Supporting Material). We perform the optical simulation by COMSOL Multiphysics based on the finite-element method (FEM). In the simulation, the optical permittivity of gold is obtained from the literature (Johnson and Christy, 1972), and the refractive index of PAH/PSS bilayer is assumed as 1.50 (Ray et al., 2007) (see Section 4 in Supporting Material).

3. Results and discussion

3.1. Plasmonic resonance effects of complementary PNP and PNH metasurfaces

For the PNP and PNH metasurfaces with two orthogonal reciprocal lattice vectors, the plasmonic resonance wavelength under normal incidence can be evaluated as below (Ghaemi et al., 1998),

$$\lambda_{SPP} = \frac{P}{\sqrt{i^2 + j^2}} \sqrt{\frac{\varepsilon_d \varepsilon_m}{\varepsilon_d + \varepsilon_m}} \quad (1)$$

where P is the period of metasurfaces, ε_d and ε_m are the dielectric functions of the environmental dielectric medium and metal, respectively, and (i, j) is the orders of plasmonic resonance modes. Equation (1) provides a good guide for analyzing the plasmonic resonance influenced by the lattice period and surrounding environmental dielectric materials, but it only refers to an ideal nanostructure lattice and neglects the effects of metasurface complementary morphologies and size differences. In order to have a better understanding of the physical effects, we perform a series of optical simulations and analyze the spectra of metasurfaces with different duty factors in Fig. 1, where the insets denote the perspective and cross-section views of metasurfaces. The duty factors of PNP and PNH metasurfaces are defined as $f_1 = D_1/P$ and $f_2 = D_2/P$, where D_1 and D_2 are the diameter of the gold nanopillars and nanoholes, respectively. In the simulation, both the height of nanopillars and the depth of nanoholes are $h = 200$ nm, and the surrounding environmental medium is water. For the two kinds of metasurfaces, when the duty factor is very small and close to zero (*e. g.* 1/24), their wavelengths of fundamental plasmonic resonance are getting closer to $\lambda = 683.5$ nm. The spectral dips of this plasmonic resonance are very tiny around this wavelength, and they would disappear, as f_1 and f_2 become zero, on which conditions the complementary metasurfaces turn to the ideal metallic thin film. When we increase f_1 and f_2 of the complementary metasurfaces from 1/24 to 13/24, the plasmonic resonance wavelength shifts from about 683.5 nm to the shorter ($\lambda = 635.0$ nm) and longer ($\lambda = 761.0$ nm) wavelengths, respectively. This can be explained by comparing the effective dielectric permittivity of the combination in the dashed squares (shown in the insets of Fig. 1). The ratio of water is reduced as we increase f_1, but it is increased as we raise f_2, which induces the effective permittivity values for the PNP and PNH metasurfaces change towards the opposite directions. A further interpretation could

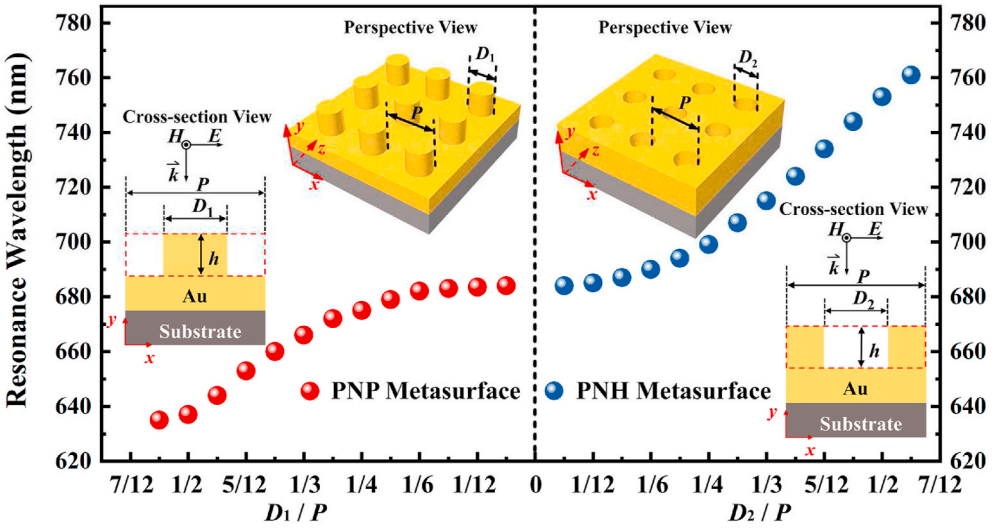

Fig. 1. Simulated resonance wavelength of PNP and PNH metasurfaces as a function of metaunit duty factor, where the insets denote the perspective and cross-section views of metasurfaces.

be also conducted by the dynamic change of positive-negative charge densities and field distributions (Chau et al., 2016, 2019b). The results in Fig. 1 demonstrate that the plasmonic resonance wavelengths of complementary metasurfaces can be tuned by changing the duty factor in a large spectral range. The plasmonic resonance wavelengths of complementary PNP and PNH metasurfaces are located on both sides of the critical wavelength of 683.5 nm, which can not be reflected by using the conventional theory based on Equation (1). In fact, the systematic simulation and analysis can be performed to investigate the influence of metasurface structural parameters on the optical properties in order to optimize the sensing performance (Chau et al., 2018, 2020). Based on the plasmonic effects of complementary metasurfaces and optical simulation, we next perform the nanofabrication and spectral measurement in experiments.

In experiments, we fabricate the complementary PNH and PNP metasurfaces simultaneously by nanoimprinting with the same nickel mold. Their structure dimensions have been separately optimized by a series of optical simulation and fabrication procedures (Zhu et al., 2020a,b; Zhou et al., 2019). Their morphologies are shown and compared in Fig. 2(a) and Fig. 2(b). Their reflectance spectra in water

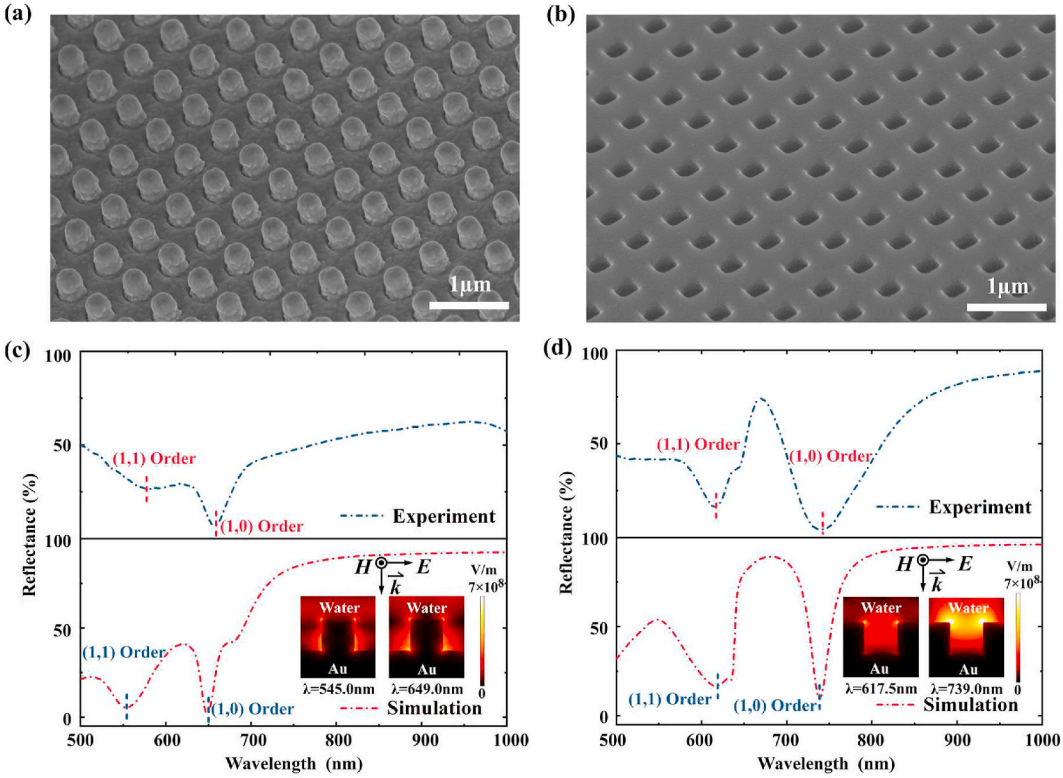

Fig. 2. SEM images of 45° oblique view for (a) PNP metasurface and (b) PNH metasurface. (c) Measured and simulated reflectance spectra of (c) PNP metasurface and (d) PNH metasurface under normal incidence in the deionized water, where the insets denote the electric field distributions for the plasmonic modes at resonance wavelengths.

are measured and compared with optical simulation results in Fig. 2(c) and (d). The experimental spectra for both the two complementary metasurfaces at normal incidence indicate the (1,0) and (1,1) order plasmonic resonance modes, and they demonstrate good consistency with the simulation results. We further plot the electric field distributions at these resonance wavelengths in the insets of Fig. 2(c) and (d). The electric fields of the (1,0) and (1,1) order resonances for the PNP metasurface are concentrated and highly confined along the nanopillar side wall, and the significant field enhancement exists at the top and bottom edges of the nanopillar. In contrast, the electric field of the (1,0) and (1,1) order resonances for the PNH metasurface are mainly concentrated and enhanced surrounding the mouth of nanohole. Particularly, the (1,0) order mode demonstrates a higher enhanced field area than the (1,1) order mode, and the (1,0) order field decay length off the largest field point at nanohole mouth is within the scale range of 100 nm. Preliminarily, by comparing the field distributions in Fig. 2(c) and (d), we can observe that the (1,0) order mode of PNH metasurface has a much more considerable enhanced field region than the other modes, which implies the promising potential for biosensing. Based on the fundamental analysis, we next focus on the SRIS comparison study of the PNP and PNH metasurfaces, which will facilitate the further evaluation of their biosensing applications.

3.2. Comparative SRIS investigation of complementary metasurfaces

Since the (1,1) order resonance of PNP metasurface is located at the wavelength of 573 nm, which is influenced by the intrinsic high material loss of gold in experiments, we mainly focus on the sensing performance comparison for the (1,0) order resonance of the two complementary metasurfaces. We first obtain their BRIS values by measuring their reflectance spectra in deionized water, ethanol, isopropanol and glycol, respectively, as shown in Fig. 3(a). The PNH metasurfaces indicate a BRIS of 485.9nm/RIU, which is about 100nm/RIU higher than that of PNP metasurfaces. We next study their SRIS for biomolecule detection by the LbL assembly method, as shown in Fig. 3(b). This method can generate the uniform conformal polymer layers with the controllable thickness. Each polyelectrolyte bilayer is composed of PAH with a positive charge and PSS with a negative charge. Here, the average thickness of the PAH/PSS bilayer is assumed to be about 2.9 nm (Liang et al., 2018). Particularly, considering the nanostructure coating by PAH/PSS bilayers, the tight covering on concave corners might be more difficult than convex corners due to the deformation effects of the assembled molecule bilayers, which could generate an incomplete conformal coating shape, as shown in Fig. 3(b) (Bendix et al., 2009). The resonance wavelength shift as a function of the PAH/PSS bilayer number is plotted in Fig. 3(c). It is observed that the wavelength shift gradually increases with the rise of the biomolecular layer number for both complementary metasurfaces. For the PNH metasurfaces, each bilayer coated on the Au metasurface leads to the spectral shift of reflectance resonance exceeding 5 nm before 4 PAH/PSS bilayers, which is an exceptionally superior sensing performance and we define the coverage of 4 PAH/PSS bilayers as a high sensitive region. When N changes from 5 to 16 (Intermediate Region), the wavelength shift per unit PAH/PSS bilayer gradually becomes smaller and smaller, and it is close to zero after N = 16 (Saturation Region). The saturated wavelength shift is ~54.3 nm. In contrast, the wavelength shifts of PNP metasurfaces reach a plateau after 16 PAH/PSS bilayers and the saturated wavelength shift is ~36.4 nm, respectively. This implies that the PNH metasurfaces have a larger near-field sensing region surrounding the surface of metastructure. The SRIS performances of two plasmonic resonance modes are analyzed by

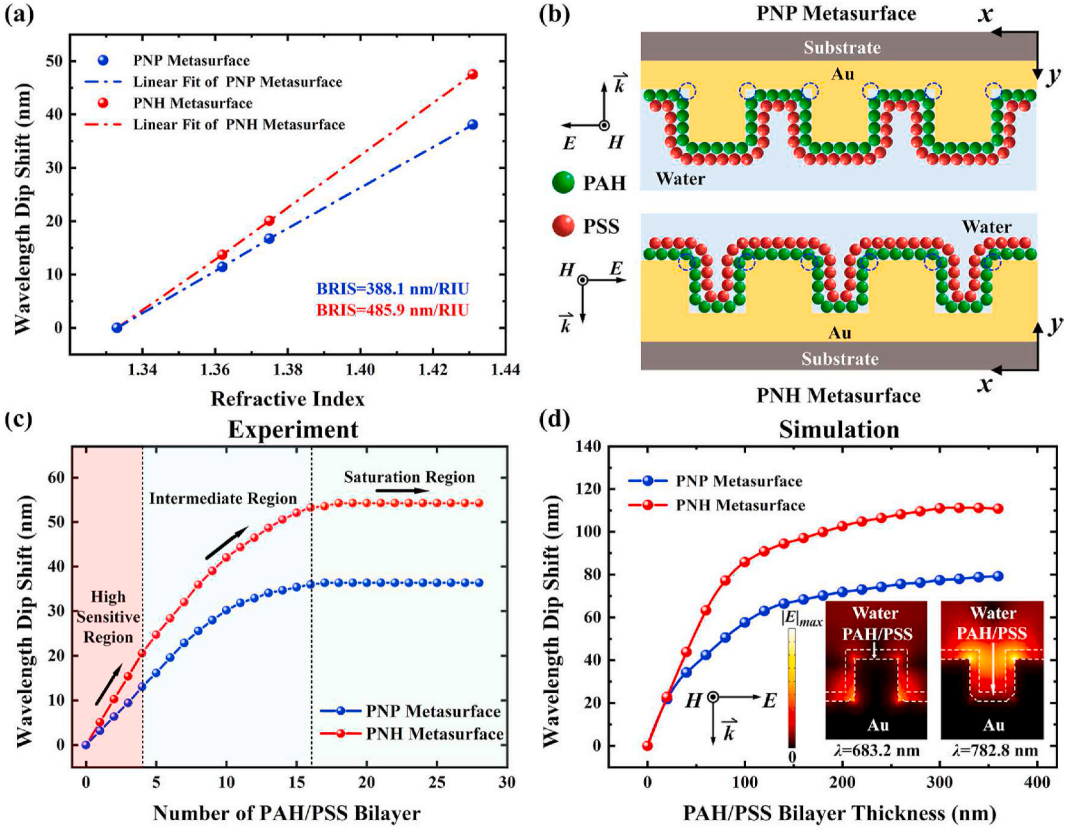

Fig. 3. (a) Resonance wavelength shift of the (1,0) mode as a function of refractive index. (b) Schematic drawing of alternating PAH/PSS bilayers on the metasurfaces, where the blue dashed circles denote the locations for the largest near-field enhancement. (c) Measured resonance wavelength shift as a function of PAH/PSS bilayer number. (d) Simulated resonance wavelength shift as a function of PAH/PSS bilayer thickness, where the insets denote the electric field distributions for the metasurfaces with 40 nm PAH/PSS bilayers.

using the full wave optical simulation. As shown in Fig. 3(d), the simulation results are in good agreement with the experimental results. The higher wavelength dip shifts and saturation spectral shifts in simulation might be due to the ideal dense conformal coating modeling of PAH/PSS with a lager effective refractive index than practice. The PAH/PSS bilayer thicknesses (above 50 nm) for saturation spectral shifts in experiments are smaller than those (above 200 nm) in the simulation. This difference is attributed to the smaller decay length of electric field on practical metasurfaces, which might originate from the actual surface roughness of fabricated samples with higher metallic damping loss (Shen et al., 2021). Despite this, the simulation results indicate that the saturation spectral shift of the PNH metasurfaces is larger than the PNP metasurfaces, which is consistent with the measuring data. We further plot their electric field distributions with 40 nm bilayers at resonance wavelengths in the insets of Fig. 3(d). Taking into account the deformation of PAH/PSS bilayers, we assume a rotator region of isosceles right triangle (a side length of 30 nm) to simulate the incomplete conformal assembly bilayers. For the PNP metasurface, the local electric field is highly confined and enhanced at the bottom edges of the nanopillar, where the assembly bilayers are not tightly attached. Such characteristic reduces the near-field utilization efficiency for biomolecules and leads to the reduction in SRIS. In contrast, the electric field of PNH metasurface is mainly concentrated surrounding the mouth of nanohole, which is conducive to increase the near-field utilization efficiency for biosensing.

In order to further study the SRIS of complementary metasurfaces in physics, we introduce the equation of plasmonic resonance wavelength shift $\Delta\lambda$ as a function of environmental optical parameters (Haes and Duyne, 2002), which is shown as below,

$$\Delta\lambda = m \times (n_{PL} - n_{ed}) \times (1 - e^{-2t/l_d}) \quad (2)$$

where m, n_{PL} and n_{ed} represent the sensitivity factor, the refractive index of PAH/PSS bilayer and the background dielectric medium, respectively. t is the thickness of the PAH/PSS bilayer, and l_d is the effective exponential decay length of the evanescent electric field. The sensitivity factor m and decay length l_d for PNP and PNH metasurfaces can be calculated by fitting Equation (2) to the results in Fig. 3(c) (see Table S1). For PNP metasurfaces, the calculated m is 323.6nm/RIU and the effective decay length l_d is 75.3 ± 2.5 nm. For PNH metasurfaces, m is 467.4nm/RIU, and l_d is 75.8 ± 1.1 nm. The calculated m factors for PNP and PNH metasurfaces are 323.6nm/RIU and 467.4nm/RIU, respectively, which are close to the corresponding experimental BRIS values of 388.1nm/RIU and 485.9nm/RIU. This result is consistent with the fact that the m values are usually close to the bulk refractive index (Jung et al., 1998; Liang et al., 2018). In addition, the calculated l_d for PNP and PNH metasurfaces are 75.3 ± 2.5 nm and 75.8 ± 1.1 nm, respectively. This indicates that the PNP and PNH metasurfaces have almost the same effective decay length, which might be due to the complementary geometry.

In order to have a more detailed comparison of SRIS, we calculate the second order mixed partial derivative of $\Delta\lambda$ for the (1,0) order resonance of complementary metasurfaces. According to the following equation,

$$\frac{\partial^2 \Delta\lambda}{\partial n \partial t} = \frac{2m}{l_d} e^{-2t/l_d} \quad (3)$$

We plot their second order SRIS as a function of surface dielectric thickness in Fig. 4(a). It can be clearly seen that both their second order SRIS exponentially reduces as t increases from 0 nm to 120 nm, whereas, the PNH metasurfaces always have a higher second order surface sensitivity for each surface dielectric thickness than the PNP metasurfaces. For $t = 0$ nm, the second order sensitivity of PNH metasurface is 3.73 RIU^{-1} higher than that of PNP metasurfaces. For $t = 120$ nm, their second order SRIS values are very small and close to each other. The red shaded area in Fig. 4(a)denotes the higher sensing performance of PNH metasurfaces in the surface near-field region, which is more promising for surface biomolecule sensing.

We next focus on comparing their biomolecule detection performance by measuring their limit of detection (LOD) and biomolecule detection sensitivity, which imply a critical criterion for further clinical applications. A standard immunoassay set of BSA/anti-BSA solutions is adopted to preliminarily evaluate their application potential. We plot the (1,0) order resonance wavelength shift as a function of anti-BSA concentrations in Fig. 4(b). The Four Parameters Logistic Regression (4 PL) equation is used to fit the experimental data. Based on the 4 PL fitting parameters (see Table S2), the LODs of PNP and PNH metasurfaces are about 0.142 ng/mL and 0.078 ng/mL, respectively. The sensitivities of PNP and PNH metasurfaces are 1.746 ng/mL and 1.300 ng/mL, respectively. This implies that PNH metasurfaces have better anti-BSA sensing performance with a lower LOD and a better biomolecular sensitivity, which is consistent with its higher second order SRIS in the test of PAH/PSS assembly bilayers. According to Fig. 4(b), the most sensitive ranges (i.e. dynamic ranges labeled by the red and blue shaded areas) of the PNP and PNH metasurfaces are mostly overlapped. In the dynamic range, the PNH metasurfaces demonstrate a higher sensitivity and a better sensing capability for low-concentration anti-BSA. Based on the investigations above, we find that the PNH metasurfaces have a higher surface near-field sensing efficiency for biomolecular detection than the PNP metasurfaces. This implies that it would be a good candidate for biomedical detection based on plasmonic nanostructures. Therefore, we next focus on the study of PNH metasurfaces for the clinical detection of biomarkers.

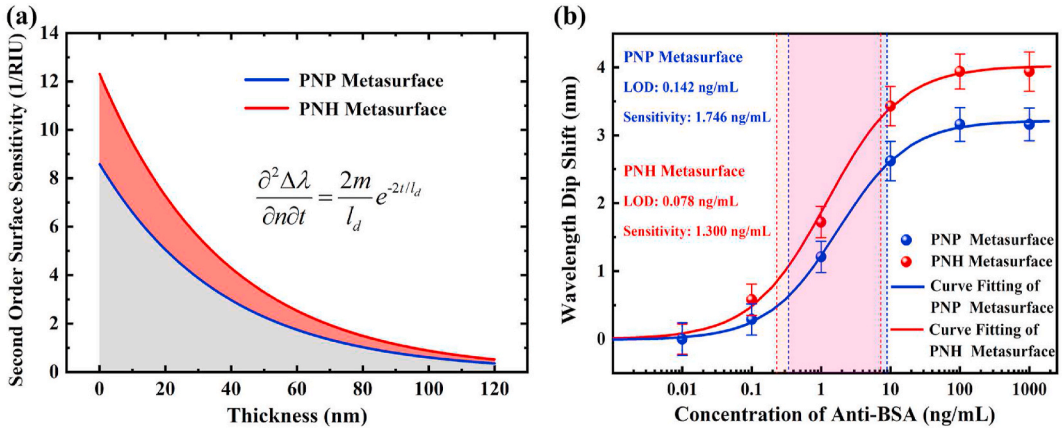

Fig. 4. (a) Comparison of the second order surface sensitivity curves for the (1,0) order resonance of metasurfaces. (b) The wavelength dip shift as a 4 PL function of anti-BSA concentration for the detection by bio-functionalized metasurfaces.

3.3. Exploring the immunodetection efficiencies of multiplex tumor markers for PNH metasurfaces

The immunodetection of multiplex tumor markers is an important way in early cancer screening. Here, we adopt the PNH metasurfaces to study the sensing efficiencies for three representative tumor markers, i.e. CA 50, CA 19-9 and AFP. In order to detect a target tumor marker, one must introduce a biofunctionalization layer followed by a capture molecule, as shown in Fig. 5(a). In view of the effective near-field decay length of PNH metasurface, the thickness of biofunctionalization layer and the sizes of capture molecule and target tumor marker as well as their refractive index will influence the sensing efficiency of tumor marker. The PNH metasurfaces for the detection of CA 50, CA 19-9 and AFP have the same biofunctionalization layers due to the same 11-Mercaptoundecanoic acid (MUA) pretreatment. This layer (Region I) along with the capture molecule (Region II) occupies the metastructure surface region with the largest near field of plasmonic mode, whereas the target molecule (Region III) could only occupy the surface region with a relatively smaller second order surface sensitivity when it is detected. On the metasurface, the intrinsic immunodetection mechanism determines the inevitable usage of the most sensitive surface region by the biofunctionalization layer and capture molecule. Since the biofunctionalization layers for detecting CA 19-9, AFP and CA 50 have the same thickness (less than 10 nm), we focus on studying the space occupation conditions of their capture/target molecule pairs in order to explore their surface sensing efficiencies. In this study, all the three capture/target molecule pairs are in the size range from about 20 nm to 30 nm (Reth, 2013), so they are kept within the decay length of the electric field ($l_d \approx 75$ nm). As shown in Fig. 5(b), we observe that the resonance wavelengths after the saturated immobilization for the antibodies of AFP, CA 19-9 and CA 50 have the redshifts of ~4.6 nm, ~6.9 nm and ~8.9 nm, respectively. These redshifts correspond to their molecular weights (see Table S3) of ~68 kDa, ~150 kDa and ~190 kDa, respectively. The molecular weights of CA 19-9 antibody and CA 50 antibody are ~2.2 times and ~2.8 times of that for the AFP antibody, respectively; whereas their spectral redshifts are ~1.5 times and ~1.9 times of that for the AFP antibody, respectively. The ratio differences between molecular weight and spectral shift might be attributed to the different steric hindrances or refractive index values among the three kinds of antibodies; nevertheless, the experimental results imply that the spectral redshift for antibody immobilization mainly depends on the size of the capture molecule.

Finally, we focus on studying the surface sensing effects of different target molecules. Based on the spectra for measuring CA 19-9, CA 50, and AFP, the resonance redshifts as a function of their concentration are plotted in Fig. 6(a–c). Each error bar of measurement is based on *s.d.* calculation for five data points. All the three data fittings have a correlation coefficient (R^2) of above 0.99, which demonstrates a good linear relationship between the antigen concentration and resonance wavelength. As shown from Fig. S6 to Fig. S8, compared with the PNH metasurfaces without biofunctionalization, the maximum measured concentrations for 95IU/mL CA 19-9, 50IU/mL CA 50, and 41.32IU/mL AFP lead to the resonance shifts of ~17.1 nm, ~19.1 nm, and ~15.3 nm, respectively. According to Fig. 3(c), the three resonance shifts are confined within the high sensitivity region of SRIS ($\Delta\lambda$ <20 nm), which ensures the optimal sensing performance. Compared with the sensing fittings in Fig. 6(a) and (b), the detection of CA 50 has a larger slope coefficient of 0.0766 versus that of CA 19-9 with 0.0252, which indicates that the detection of CA 50 has a much better sensitivity. This is because the detection of CA19-9 and CA 50 adopts close antibody molecular weights (~150 kDa and ~190 kDa), but the molecular weight of CA19-9 (~10 kDa) is much smaller than CA 50 (~210 kDa). CA 50 with a larger molecular size can occupy the near-field decay length region of metasurface much more effectively than CA 19-9. We further compare the sensing performance of CA 50 and AFP in Fig. 6(b) and (c). Interestingly, the ~70 kDa AFP has a larger slope coefficient of 0.1091 than the CA 50 (~210 kDa). This is mainly due to the big size difference between the antibodies of AFP and CA 50 (~68 kDa and ~190 kDa), which implies that the antibody of AFP takes a smaller decay length region that can be more effectively utilized by the detection of AFP target molecule. Therefore, the AFP with appropriate antibody/antigen molecule pairs maintains the highest biomolecular detection sensitivity. In order to ensure high sensitivity in practice, it is very beneficial to use the capture molecule with a smaller size and the target molecule with a larger size.

We further adopt the antibody-immobilized PNH metasurfaces for clinical applications, and the serum samples for different concentrations of CA 19-9, CA 50, and AFP from The First Affiliated Hospital of Xiamen University (Xiamen, China) are tested. We first confirm the good antigen detection specificity of our sensing devices by the serum samples (see Fig. S9). After that we compare the detected antigen concentration results with those measured by chemiluminescent immunoassay (CLIA) in the hospital. As shown from Fig. 6(d)–6(f), the detection tests for CA 19-9, CA 50 and AFP in serum samples by PNH metasurfaces demonstrate good consistency with the results by CLIA (the coefficient of variation is shown from Table S4 to Table S6), and the metasurfaces show the capability to detect antigen concentrations lower than the clinical diagnosis thresholds for the three kinds of tumor markers (37 IU/mL, 17 IU/mL and 16.5 IU/mL for CA 19-9, CA 50 and AFP, respectively) (Paganuzzi et al., 1988; Tayob et al., 2016). Among these clinical serum tests, the set of experiments for AFP demonstrates the best capability to detect the lowest antigen concentration (less than 5 IU/mL), which is

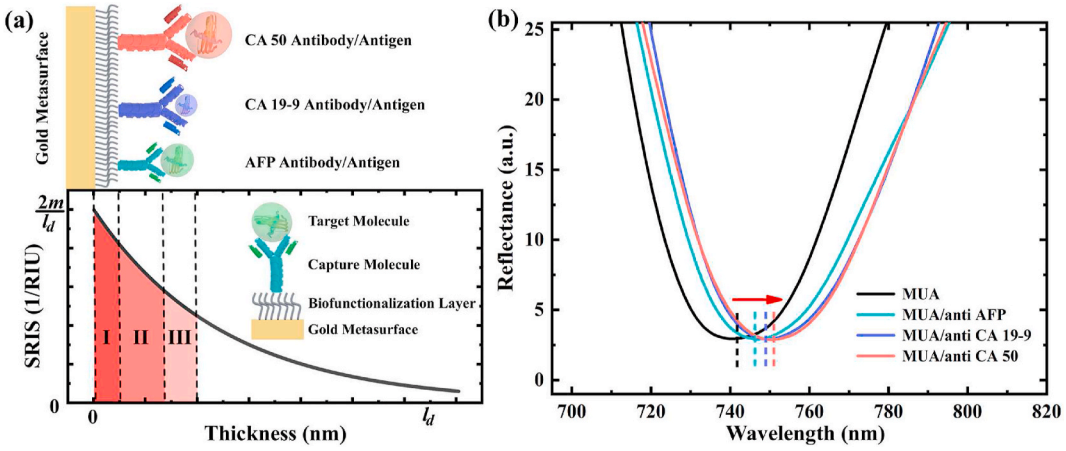

Fig. 5. (a) The SRIS of PNH metasurfaces for three kinds of capture/target molecule pairs. (b) Reflectance spectra for bond antibodies in PNH metasurfaces with different molecular weights.

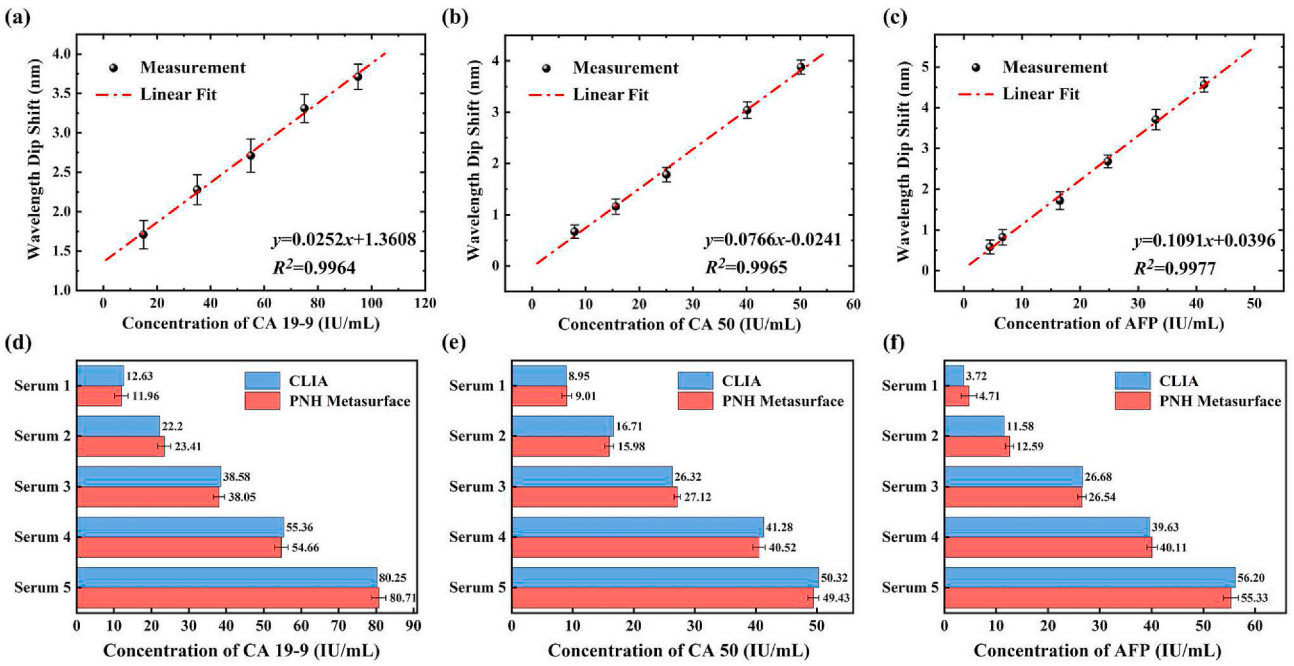

Fig. 6. PNH metasurface resonance wavelength shift as a function of antigen concentration for (a) CA 19-9, (b) CA 50 and (c) AFP. The symbols y and R^2 denote the linear fitting function and correlation coefficient, respectively. Serum detection results of (d) CA 19-9, (e) CA 50 and (f) AFP.

well in agreement with the sensitivity result (the largest slope coefficient from Fig. 6(a)–6(c)). This result further indicates that the detection for AFP covers a wide sensing concentration for the antigen (especially for the low concentration), which is attributed to the highest near-field sensing efficiency of the anti-AFP/AFP immunodetection scheme. These experiments show the promising potential of PNH metasurfaces for point-of-care-testing, and designate an explicit way to enhance the sensing performance in the plasmonic immunodetection mechanism.

4. Conclusions

In summary, we systematically study the complementary PNP and PNH metasurfaces and compare their plasmonic biosensing performance. The PNH metasurfaces demonstrate a larger near-field sensing region and imply superior biosensing performance. Their immunodetection experiments show that the AFP with the appropriate antibody/antigen size maintains the highest near-field utilization efficiency for sensing. Our method is confirmed by testing human serum samples, thus paving a reliable way for detecting various tumor markers. Our metasurfaces adopt the noble metal gold, which could be expensive for the commercialization of disposable biosensors. We will do further investigations by using low-cost raw materials in the future work.

CRediT authorship contribution statement

Fajun Li: Methodology, Software, Formal analysis, Validation, Investigation, Data curation, Visualization, Writing – original draft, Writing – review & editing. **Jiaqing Shen:** Software, Validation, Investigation, Data curation, Writing – original draft. **Chaoheng Guan:** Validation, Investigation, Data curation. **Yinong Xie:** Methodology, Software, Formal analysis. **Zhenbiao Wang:** Validation, Investigation. **Shaowei Lin:** Data curation, Validation. **Junjie Chen:** Investigation, Writing – review & editing. **Jinfeng Zhu:** Conceptualization, Methodology, Resources, Validation, Formal analysis, Investigation, Visualization, Supervision, Writing – review & editing, Project administration, Funding acquisition.

Declaration of competing interest

The authors declare that they have no known competing financial interests or personal relationships that could have appeared to influence the work reported in this paper.

Acknowledgement

This work was supported by NSFC (62175205), NSAF (U2130112, U1830116), the Fujian Provincial Natural Science Foundation of China (2020J06009), the Open Fund of State Key Laboratory of Applied Optics (SKLAO2020001A15), Xiamen Municipal Bureau of Science and Technology (3502Z20203006) and Fundamental Research Funds for the Central Universities (20720190010).

Appendix A. Supplementary data

Supplementary data to this article can be found online at https://doi.org/10.1016/j.bios.2022.114038.

References

Belushkin, A., Yesilkoy, F., Altug, H., 2018. ACS Nano 12, 4453–4461.
Bendix, P.M., Pedersen, M.S., Stamou, D., 2009. Proc. Natl. Acad. Sci. Unit. States Am. 30, 12341–12346.
Cai, J., Zhang, C., Liang, C., Min, S., Cheng, X., Li, W.D., 2019. Adv. Opt. Mater. 7, 1900516.
Chau, Y.F.C., Chen, K.H., Chiang, H.P., Lim, C.M., Huang, H.J., Lai, C.H., Kumara, N.T.R. N., 2019a. Nanomaterials 9, 1691.
Chau, Y.F.C., Lim, C.M., Lee, C., Huang, H.J., Lin, C.T., Kumara, N.T.R.N., Yoong, V.N., Chiang, H.-P., 2016. J. Appl. Phys. 120, 093110.
Chau, Y.F.C., Chou Chao, C.T., Huang, H.J., Anward, U., Lim, C.M., Voo, N.Y., Mahadi, A. H., 2019b. Results Phys. 15, 102567.
Chau, Y.F.C., Chou Chao, C.T., Lim, C.M., Huang, H.J., Chiang, H.P., 2018. ACS Omega 3, 7508–7516.
Chau, Y.F.C., Chou Chao, C.T., Huang, H.J., Kooh, M.R.R., Kumara, N.T.R.N., Lim, C.M., Chiang, H.-P., 2020. Nanomaterials 10, 493.
Chou Chao, C.T., Chou Chau, Y., Huang, H.J., Kumara, N.T.R.N., Kooh, M.R.R., Lim, C. M., Chiang, H.-P., 2020. Nanomaterials 10, 1399.
Couture, M., Live, L.S., Dhawanb, A., Masson, J.F., 2012. Analyst 137, 4162.
Gao, M., Yang, W., Wang, Z., Lin, S., Zhu, J., Yang, Z., 2020. Photon. Res. 8, 1226–1235.
Ghaemi, H.F., Thio, T., Grupp, D.E., Ebbesen, T.W., Lezec, H.J., 1998. Phys. Rev. B 58, 6782–6799.

Hackett, L.P., Ameen, A., Li, W., Dar, F.K., Goddard, L.L., Liu, G.L., 2018. ACS Sens. 3, 290–298.
Haes, A.J., Duyne, R.P.V., 2002. J. Am. Chem. Soc. 124, 10596–10604.
He, K., Xiao, S., Zhu, J., 2021. IEEE J. Sel. Top. Quant. 27 (5), 6900506.
Huang, L., Ding, L., Zhou, J., Chen, S., Chen, F., Zhao, C., Xu, J., Hu, W., Ji, J., Xu, H., Liu, G.L., 2021. Biosens. Bioelectron. 171, 112685.
Im, H., Shao, H., Park, Y.I., Peterson, V.M., Castro, C.M., Weissleder, R., Lee, H., 2014. Nat. Biotechnol. 32 (5), 490–495.
Jiao, F., Li, F., Shen, J., Guan, C., Khan, S.A., Wang, J., Yang, Z., Zhu, J., 2021. Sensor. Actuator. B Chem. 344, 130170.
Johnson, P.B., Christy, R.W., 1972. Phys. Rev. B 6 (12), 4370.
Jung, L.S., Campbell, C.T., Chinowsky, T.M., Mar, M.N., Yee, S.S., 1998. Langmuir 7463, 5636–5648.
Kedem, O., Tesler, A.B., Vaskevich, A., Rubinstein, I., 2011. ACS Nano 5 (2), 748–760.
Ko, J., Park, S.G., Lee, S., Wang, X., Mun, C., Kim, S., Kim, D.H., Choo, J., 2018. ACS Appl. Mater. Interfaces 10, 6831–6840.
Lee, J.U., Kim, W.H., Lee, H.S., Park, K.H., Sim, S.J., 2019. Small 15, 1804968.
Li, J., Ye, J., Chen, C., Li, Y., Verellen, N., Moshchalkov, V.V., Lagae, L., Dorpe, P.V., 2015. ACS Photonics 2, 425–431.
Li, W., Jiang, X., Xue, J., Zhou, Z., Zhou, J., 2015. Biosens. Bioelectron. 68, 468–474.
Liang, Y., Li, L., Lu, M., Yuan, H., Long, Z., Peng, W., Xu, T., 2018. Nanoscale 10, 548–555.
Liu, B., Chen, S., Zhang, J., Yao, X., Zhong, J., Lin, H., Huang, T., Yang, Z., Zhu, J., Liu, S., Lienau, C., Wang, L., Ren, B., 2018. Adv. Mater. 30, 1706031.
Mariani, S., Robbiano, V., Strambini, L.M., Debrassi, A., Egri, G., Dähne, L., Barillaro, G., 2018. Nat. Commun. 9, 5256.
Oh, S.H., Altug, H., 2018. Nat. Commun. 9, 5263.
Paganuzzi, M., Onetto, M., Marroni, P., Barone, D., Conio, M., Aste, H., Pugliese, V., 1988. Cancer 61, 2100–2108.
Prasad, A., Choi, J., Jia, Z., Park, S., Gartia, M.R., 2019. Biosens. Bioelectron. 130, 185–203.
Ray, D., Raziman, T.V., Santschi, C., Etezadi, D., Altug, H., Martin, O.J.F., 2020. Nano Lett. 20, 8752–8759.
Ray, K., Badugu, R., Lakowicz, J.R., 2007. Chem. Mater. 19, 5902–5909.
Reth, M., 2013. Nat. Immunol. 14, 765–767.
Shen, Y., He, K., Zou, Q., Xing, S., Huang, J., Zheng, M., She, X., Jin, C., 2021. Adv. Funct. Mater. 2108741.
Shen, Y., Zhou, J., Liu, T., Tao, Y., Jiang, R., Liu, M., Xiao, G., Zhu, J., Zhou, Z.K., Wang, X., Jin, C., Wang, J., 2013. Nat. Commun. 4, 2381.
Siddique, R.H., Kumar, S., Narasimhan, V., Kwon, H., Choo, H., 2019. ACS Nano 13, 13775–13783.
Špačková, B., Wrobel, P., Bocková, M., Homola, J., 2016. Proc. IEEE 104 (12), 2380–2408.
Spitzberg, J.D., Zrehen, A., van Kooten, X.F., Meller, A., 2019. Adv. Mater. 31, 1900422.
Tobing, L.Y.M., Soehartono, A.M., Mueller, A.D., Yong, K.T., Fan, W., Zhang, D.H., 2021. Nanoscale 13, 4092.
Tayob, N., Lok, S.F., Do, K.A., Feng, Z., 2016. Clin. Gastroenterol. Hepatol. 14 (3), 469–475.
Vala, M., Ertsgaard, C.T., Wittenberg, N.J., Oh, S.H., 2019. ACS Sens. 4, 3265–3274.
Wang, Y., Ali, M.A., Chow, E.K.C., Dong, L., Lu, M., 2018. Biosens. Bioelectron. 107, 224–229.
Yesilkoy, F., Terborg, R.A., Pello, J., Belushkin, A.A., Jahani, Y., Pruneri, V., Altug, H., 2018. Light Sci. Appl. 7, 17152.
Zhan, C., Liu, B.W., Tian, Z.Q., Ren, B., 2020. J. Am. Chem. Soc. 142, 10905–10909.
Zhang, L., Fu, Q., Tan, Y., Li, X., Deng, Y., Zhou, Z., Zhou, B., Xia, H., Chen, H., Qiu, C., Zhou, J., 2021. Nano Lett. 21, 2681–2689.
Zhou, J., Tao, F., Zhu, J., Lin, S., Wang, Z., Wang, X., Ou, J.Y., Li, Y., Liu, Q.H., 2019. Nanophotonics 8 (2), 307–316.
Zhu, J., Wang, Z., Lin, S., Jiang, S., Liu, X., Guo, S., 2020a. Biosens. Bioelectron. 150, 111905.
Zhu, J., Chen, X., Xie, Y., Ou, J.Y., Chen, H., Liu, Q.H., 2020b. Nanophotonics 9 (1), 167–176.